JOURNAL OF GEOPHYSICAL RESEARCH, VOL. 99, NO. C7, PAGES 14,173–14,185, JULY 15, 1994

The equatorial Kelvin wave in finite difference models

Max K.F. Ng and William W. Hsieh

Department of Oceanography, University of British Columbia, Vancouver, Canada

Abstract. Coarse resolution ocean models tend to poorly resolve many smaller-scale phenomena, including the equatorial currents narrowly confined around the equator. We study the free equatorial Kelvin wave in inviscid finite difference models using the Arakawa A, B, C, and E grids. Exact analytic solutions with meridional velocity $v = 0$ are found on the A, C, and E grids. As the assumption $v = 0$ is not valid on the B grid, the solution is obtained numerically by a "shooting" method. In all cases, the wave remains nondispersive, and the phase speed is unchanged from that in the continuum except in the B grid, where it decreases with worsening resolution. The mean zonal heat transport by the Kelvin wave during an El Niño is compared on the various grids. In terms of the currents and sea level displacements, the B grid best models the equatorial Kelvin wave under coarse resolution, though in terms of zonal heat transport and phase velocity, the C grid appears superior. The A and E grids appear to have the most trouble. Our theoretical predictions are checked experimentally by generating equatorial Kelvin waves in linear shallow-water equation models on the various grids. Additional effects of Rayleigh damping and Newtonian cooling are studied in the appendix.

1. Introduction

Distortions by finite difference effects are significant in coarse resolution ocean models, where the grid spacing is usually insufficient for properly resolving the internal Rossby radius. Nevertheless, there have only been a few studies of finite difference effects in ocean models: *Arakawa and Lamb* [1977] and *Batteen and Han* [1981] examined finite difference effects on Poincaré waves, *Henry* [1981] and *Hsieh et al.* [1983] on coastal Kelvin waves, *Wajsowicz* [1986] on Rossby waves, *Foreman* [1987] on continental shelf waves, and *O'Brien and Parham* [1992] on equatorial Kelvin waves.

Global ocean climate models and coupled climate models tend to use grid spacings of the order of the internal equatorial Rossby radius (about 290 km), which is inadequate for resolving in the meridional direction the equatorial Kelvin wave and the equatorial undercurrent, as both are trapped mainly within one Rossby radius of the equator. The zonal grid spacing, on the other hand, has a negligible effect, as the wavelength in the zonal direction is generally much larger than the Rossby radius. Henceforth we limit our study to only finite difference effects in the meridional direction. Since the equatorial Kelvin wave has a central role in determining the equatorial climatology as well as the El Niño-Southern Oscillation in climate models, the study of finite difference effects on the Kelvin wave is crucial to understanding biases in our climate models.

In finite difference ocean models, there are several possible arrangements of the model variables in the horizontal plane (Figure 1). Except for the rarely used Arakawa A grid, the grids in Figure 1 are staggered, in that the variables are not all located at the same site. The Geophysical Fluid Dynamics Laboratory (GFDL) modular ocean model and its predecessors [e.g., *Bryan and Cox*, 1967] and the *Oberhuber* [1990] model used the B grid; *Bleck and Boudra* [1981], *Blumberg and Mellor* [1983], *Dietrich et al.* [1987], and *Haidvogel et al.* [1991] used the C grid; while *Maier-Reimer and Hasselmann* [1987] used the E grid. The only previous study on finite difference effects on the equatorial Kelvin wave is a note by *O'Brien and Parham* [1992], examining a particular case of the C grid.

Our objective is to provide a comprehensive treatment of the finite difference effects on the equatorial Kelvin wave over the various grids. We present exact analytical solutions of the free equatorial Kelvin wave in the A, C, and E grids, and examine how resolution affects the wave structure and the zonal heat transport. As the B grid does not lend itself to exact analytical treatment, a numerical treatment is used for the B grid. Comparisons are made between the various grids to determine which grid models a particular aspect of the equatorial Kelvin wave best.

The outline of this paper is as follows: After laying down the governing equations in section 2, we explore equatorial Kelvin waves on the C grid in section 3, the E and A grids in section 4, and the B grid in section 5. Zonal heat transports on the various grids are compared in section 6. Our theoretical predictions are tested experimentally in section 7 by generating equatorial Kelvin waves in shallow-water equation models. Kelvin waves under Raleigh damping and Newtonian cooling in finite difference models are studied in the appendix.

2. Governing Equations

The unforced linearized shallow water equations on the equatorial β plane are

$$\begin{aligned} u_t - \beta y v &= -g'\eta_x - \varepsilon u, \\ v_t + \beta y u &= -g'\eta_y - \varepsilon v, \\ \eta_t + H(u_x + v_y) &= -\gamma\eta, \end{aligned} \tag{1}$$

where u and v are the eastward and northward velocity

Paper number 94JC00473.
0148-0227/94/94JC-00473$05.00

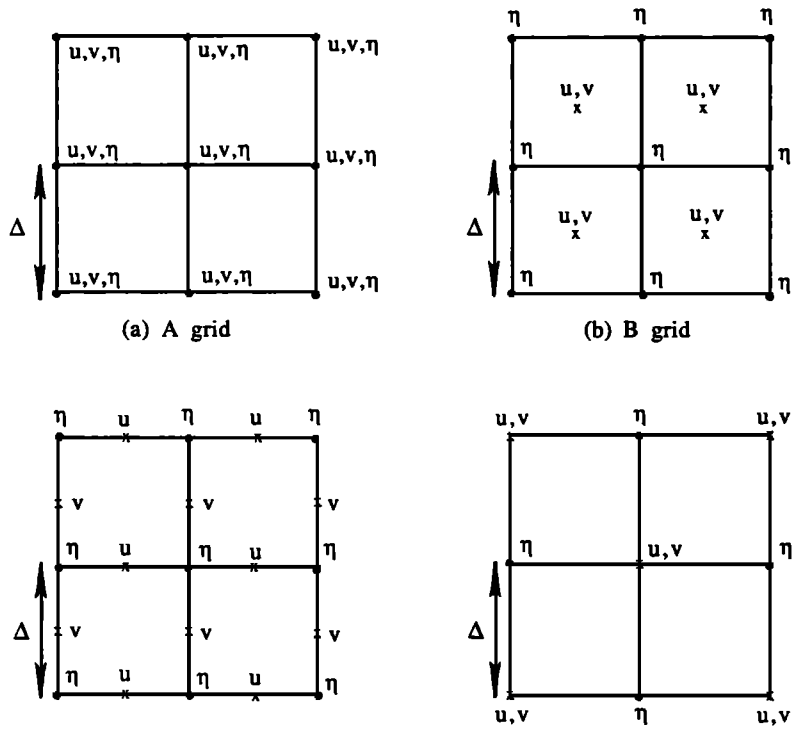

Figure 1. Orientation of the model variables in the Arakawa A, B, C, and E grids, where u, v represent the eastward and northward velocity components, and η the vertical displacement or the pressure fluctuation. Tracers such as temperature or salinity are also located at the η sites. (The ill-behaved D grid resembles the C grid, but with the u and v points interchanged). The meridional grid spacing Δ is nondimensionalized by the Rossby radius. The zonal grid spacing is irrelevant, as we will make the assumption that the zonal wavelength is well resolved by the zonal grid spacing, thus ignoring the finite difference effects in the zonal direction.

components, η the vertical displacement, β the northward derivative of the Coriolis parameter at the equator, g' the reduced gravity, H the equivalent depth, and ε and γ the coefficients for mixing of momentum and heat respectively. Equation (1) can represent either one of the internal modes in a continuously stratified fluid (*McCreary*, 1981], or the internal mode in a two-layer fluid (*Gill*, 1982], where η becomes the interface displacement. *Arakawa and Lamb* [1977] showed how the shallow water equations are computed on the various finite difference grids.

Restricting to zonal flows, we set $v = 0$. With the horizontal length scale L the equatorial Rossby radius $\sqrt{c'/\beta}$, time scale $(c'\beta)^{-1}$, and vertical length scale H, where $c'=\sqrt{g'H}$, we obtain the nondimensionalized equations

$$u_t = -\eta_x - \varepsilon u, \quad yu = -\eta_y, \quad \eta_t + u_x = -\gamma\eta, \qquad (2)$$

where (u, v) is the nondimensionalized velocity transport (velocity multiplied by the equivalent depth), and ε and γ are the nondimensionalized mixing coefficients.

We begin with the undamped case where the Rayleigh friction coefficient ε and Newtonian cooling coefficient γ are zero, so (2) reduces to

$$u_t = -\eta_x, \quad yu = -\eta_y, \quad \eta_t = -u_x. \qquad (3)$$

Assuming a plane wave solution in the zonal direction, the dynamic variables take the form of

$$[u, \eta] = [u(y), \eta(y)]\exp[i(kx - \omega t)]. \qquad (4)$$

Substituting (4) into (3) yields

$$\eta = cu, \quad yu = -cu_y, \quad c = \omega/k = \pm 1. \qquad (5)$$

The equatorially trapped solution, the equatorial Kelvin wave, follows from choosing c=1; whence

$$u(y) = u_o \exp(-y^2/2), \qquad (6)$$

with u_o the wave amplitude at the equator. The wave is nondispersive and eastward propagating, as the phase speed c = 1. Equations (5) and (6) provide the continuum solution, against which the finite difference solutions of the following sections will be compared.

3. Equatorial Kelvin Waves on the C Grid

The finite difference effect on (3) is next investigated by looking at two different configurations of the C grid (Figure 2), where the finite difference effects in the zonal direction have been ignored. A possible arrangement of the C grid places a u point on the equator (Figure 2a). Substituting (4) into the center-differenced form of the first and last equations in (3) on this C_1 grid yields

$$\omega u_j = k\eta_j, \qquad \omega\eta_j = ku_j, \qquad (7)$$

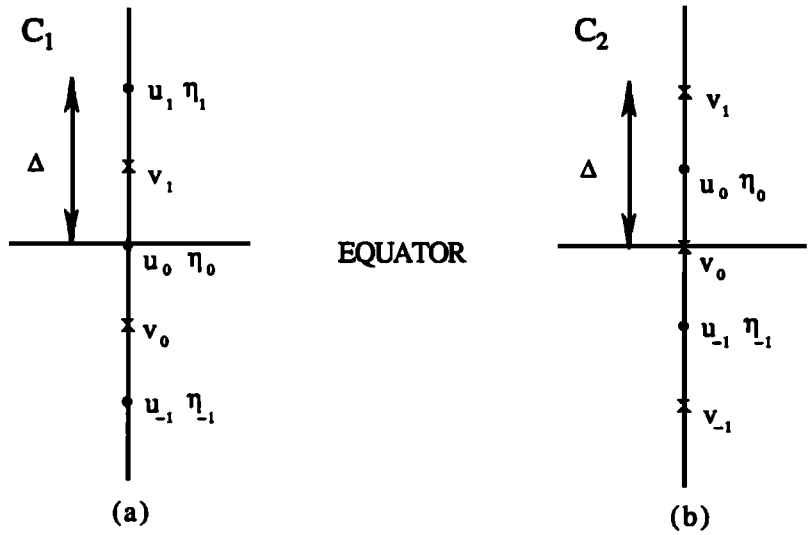

Figure 2. Two possible configurations of the C grid about the equator, henceforth referred to as the C_1 and C_2 grids, respectively.

with j the northward index defined by $y = j\Delta$ (j=0, ±1,±2...). The middle equation in (3) can be evaluated in two possible ways, depending on how the Coriolis term is approximated: case C_{1a},

$$(j-\tfrac{1}{2})\Delta\tfrac{1}{2}(u_j+u_{j-1})=-(\eta_j-\eta_{j-1})/\Delta, \qquad (8a)$$

and case C_{1b},

$$\Delta\tfrac{1}{2}[ju_j+(j-1)u_{j-1}]=-(\eta_j-\eta_{j-1})/\Delta, \qquad (8b)$$

where in case C_{1a}, the Coriolis parameter is estimated at a v point, then multiplied by the latitudinal average of two u points; whereas in case C_{1b}, the average of the Coriolis term yu at two u points is used instead. These two cases correspond respectively to the potential-enstrophy-conserving scheme and the energy-conserving scheme by *Sadourny* [1975a,b], who found that the potential-enstrophy-conserving scheme (i.e., our case C_{1a}) to have superior stability.

From (7), we have

$$\eta_j = cu_j, \qquad c=\pm 1, \qquad (9)$$

where for the eastward propagating Kelvin wave, we choose c = 1. Hence, the Kelvin wave phase speed is unaffected by the finite difference effects in the C_1 grid. Equations (9) and (8a) yield the recurrence relation

$$u_j=\left[\frac{1-(j-\frac{1}{2})\Delta^2/2c}{1+(j-\frac{1}{2})\Delta^2/2c}\right]u_{j-1}, \qquad (10)$$

case C_{1a}, where given, say, the value u_0, all other values u_j are obtained. As in the case of the continuum solution (6), the finite difference solution is also symmetric about the equator, since $u_{-j}=u_j$. In the C_{1b} case, (9) and (8b) yield

$$u_j=\left[\frac{1-(j-1)\Delta^2/2c}{1+j\Delta^2/2c}\right]u_{j-1}, \qquad (11)$$

which is also symmetric about the equator.

On the C_2 grid (Figure 2b), Equation (7) remains valid but Equations (8a) and (8b) are changed, yielding, case C_{2a},

$$u_j=\left[\frac{1-j\Delta^2/2c}{1+j\Delta^2/2c}\right]u_{j-1}, \qquad (12)$$

and case C_{2b},

$$u_j=\left[\frac{1-(j-\frac{1}{2})\Delta^2/2c}{1+(j+\frac{1}{2})\Delta^2/2c}\right]u_{j-1}, \qquad (13)$$

where the Coriolis terms are again treated in two ways, analogous to cases C_{1a} and C_{1b}, respectively. Note that the phase speed c of the equatorial Kelvin wave in all four C grid configurations is independent of the grid spacing Δ, a result analogous to the coastal Kelvin wave on the C grid as found by *Hsieh et al.* [1983]. *O'Brien and Parham* [1992] examined case C_{2a}, and essentially derived (12).

The meridional structure of u for the four cases at resolution Δ = 1 is shown in Figure 3, where the curves have been normalized to all have the same meridionally integrated zonal mass transport as in the continuum solution. In Figure 3a, the value of u in case C_{1a} is higher than that for the continuum solution at the equator, but declines away from the equator at a greater rate than the continuum solution, yielding a weak reverse flow by 3 Rossby radii from the equator. The solution in case C_{1b} is closer to that in the continuum. Similarly, Figure 3b shows that the solution in C_{2b} is better than the solution in C_{2a}. Hence for both the C_1 and C_2 configurations, method b (i.e., latitudinally averaging the Coriolis term yu from two u points) yields a more accurate equatorial Kelvin wave than method a (i.e., multiplying the Coriolis parameter at a v point to the average of two u points), despite *Sadourny's* [1975a,b] finding that method a offered superior stability. The percentage error of the finite difference solutions with respect to the continuum solution at Δ = 1 is shown in Figure 4, where results from other grids (discussed in the following sections) are also plotted to allow

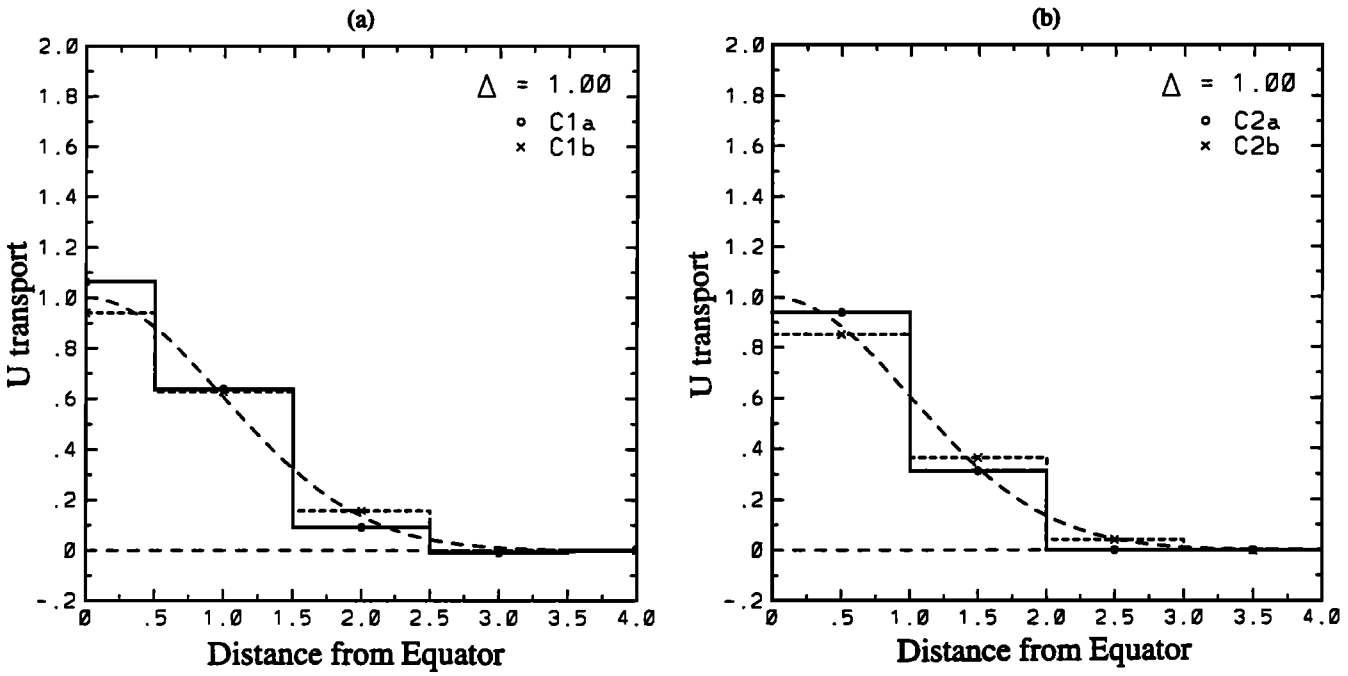

Figure 3. The zonal transport u as a function of the distance from the equator (nondimensionalized by the equatorial Rossby radius) in (a) C_{1a} (solid curve), C_{1b} (short dash curve) and the continuum (long dash curve), and (b) C_{2a} (solid curve), C_{2b} (short dash curve) and the continuum (long dash curve). These curves have all been normalized so that the total meridionally integrated u transport (i.e., area under the curve) is the same for all the curves. The grid resolution $\Delta = 1$ (where Δ is defined as the latitudinal grid spacing divided by the Rossby radius).

an intercomparison among the various grids. The changes in the zonally averaged rms error of u and h with changes in the grid resolution Δ are shown in Figure 5.

For large enough j, all four cases, i.e., (10) to (13), yield $u_j \approx -u_{j-1}$, i.e., a grid-scale oscillation always occurs in the C grid when far enough away from the equator. How far away from the equator when this oscillation occurs is controlled by Δ. For large enough Δ, the grid-scale oscillations occur right near the equator, analogous to the coastal Kelvin wave behavior found by *Hsieh et al.* [1983]. Fortunately, the Rossby radius is so much larger in the equatorial region than at midlatitudes that this pathological equatorial Kelvin wave is not likely to occur even in coarse resolution climate models.

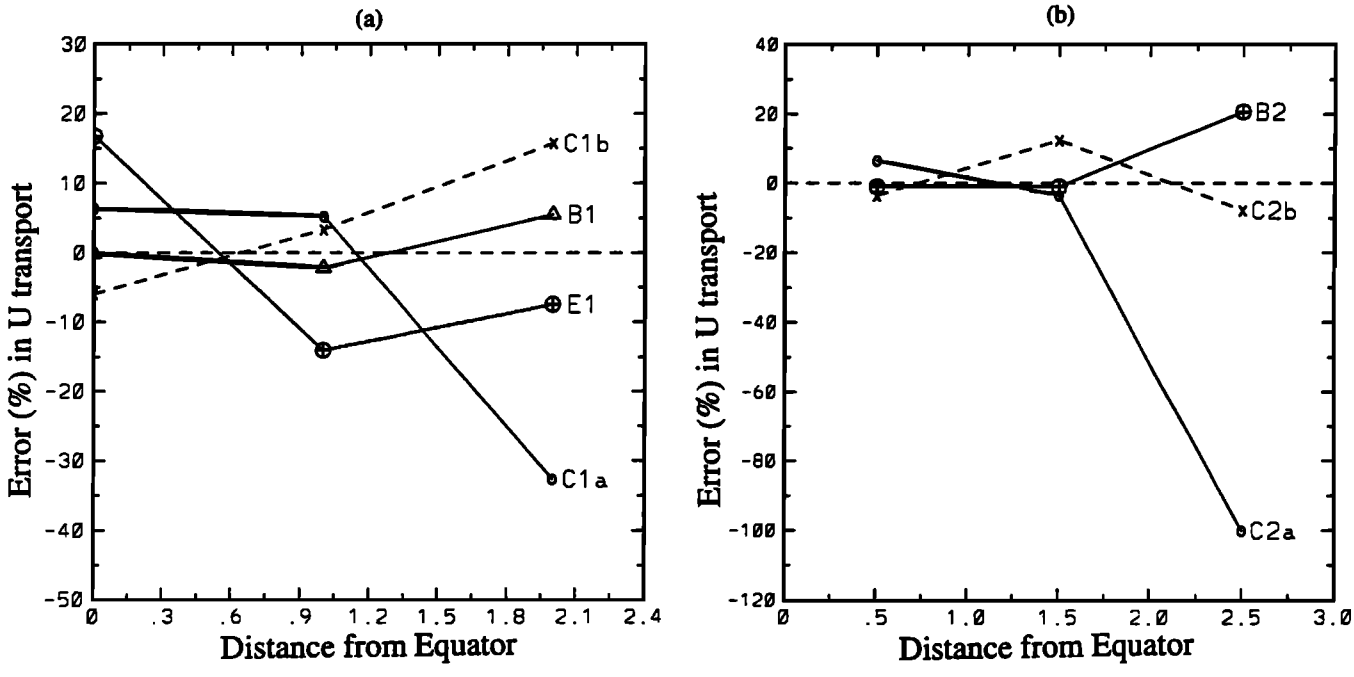

Figure 4. The percentage error in the finite difference solution of u with respect to the continuum solution for cases (a) C_{1a} (circles), C_{1b} (crosses), E_1 (circled crosses), and B_1 (triangles), and (b) for C_{2a} (circles), C_{2b} (crosses), and B_2 (circled crosses), with grid resolution Δ =1.

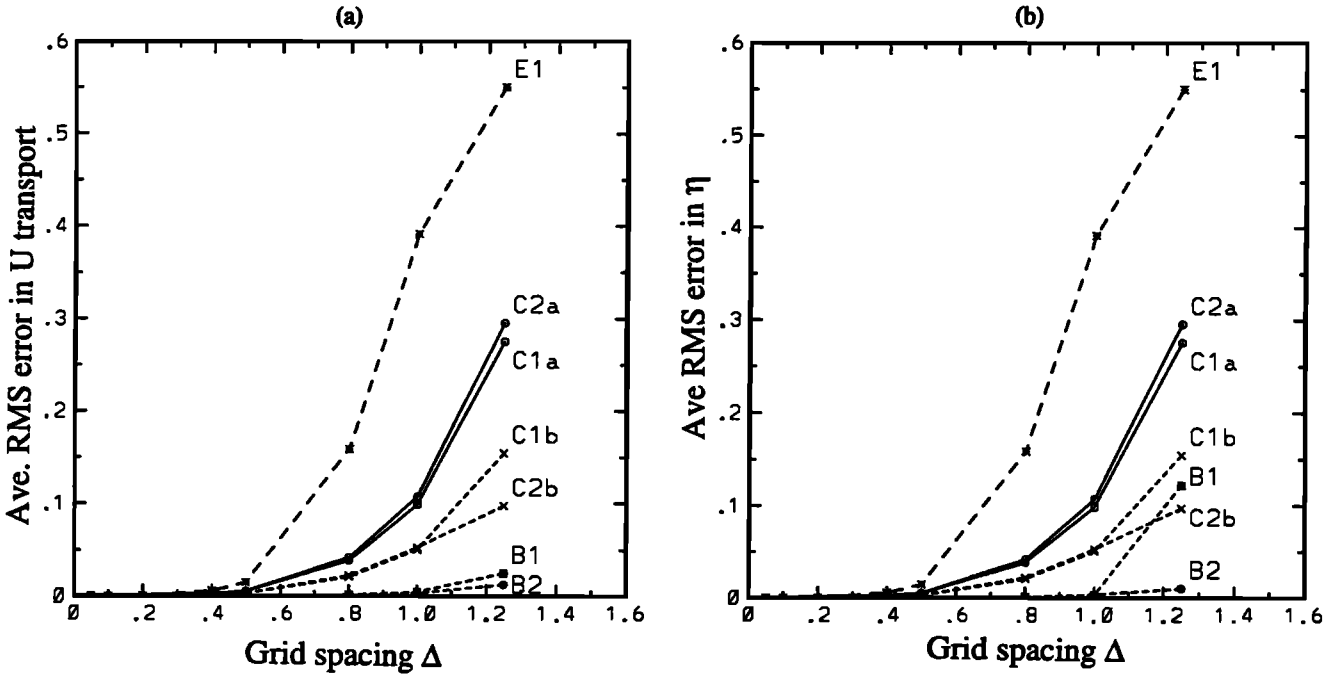

Figure 5. The zonally averaged Rms error for (a) the zonal transport u and (b) the sea level displacement h of the finite differenced equatorial Kelvin wave (with respect to that in the continuum) plotted as a function of the grid spacing Δ on the four C grids, the E_1, the B_1, and B_2 grids.

4. Equatorial Kelvin Waves on the E and A Grids

When finite difference effects in the zonal direction are ignored, the E and A grids from Figure 1 collapse to the same grid shown in Figure 6. A u point is located on the equator in the E_1 grid, where the finite difference form of (3) is given by

$$\omega u_j = k\eta_j, \qquad \omega\eta_j = ku_j, \tag{14}$$

$$j\Delta u_j = -\frac{(\eta_{j+1}-\eta_{j-1})}{2\Delta}. \tag{15}$$

Equation (14) again leads to (9), and the following recursion relation is derived:

$$u_{j+1}+\frac{2j}{c}\Delta^2 u_j - u_{j-1} = 0, \qquad (j=0, \pm1, \pm2\ldots). \tag{16}$$

In contrast to the first-order linear difference equations encountered in the previous section on the C grid, Equation (16) is a second-order linear difference equation with a nonconstant coefficient, as j is the independent variable.

A helpful hint in solving (16) is provided by the recurrence relation of the modified Bessel functions [*Abramowitz and Stegun*, 1972]:

$$F_{j+1}(z)+\frac{2j}{z}F_j(z)-F_{j-1}(z)=0, \tag{17}$$

where the argument z may be complex. When j is an integer,

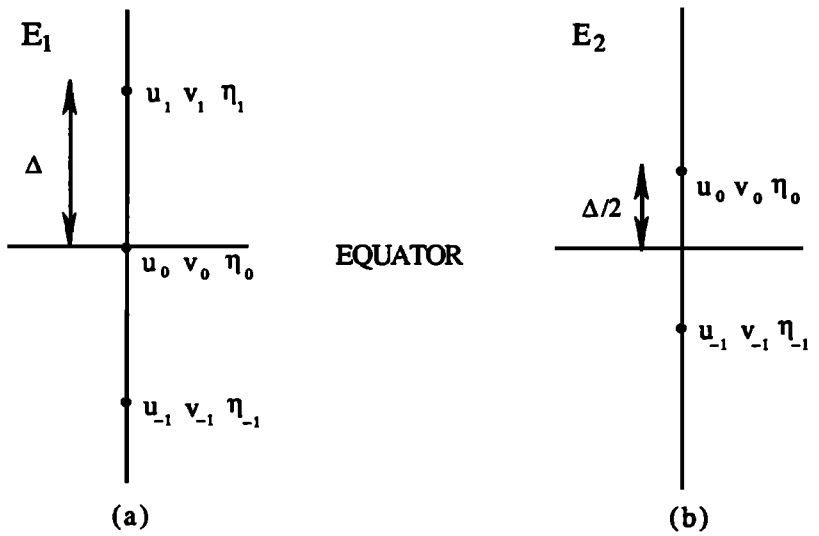

Figure 6. Two possible configurations of the E grid (or A grid) about the equator; henceforth referred to as the E_1 and E_2 grids, respectively.

the two linearly independent solutions of (17) are the modified Bessel function of the first kind, I_j, and $(-1)^j K_j$, with K_j the modified Bessel function of the second kind. Hence, F_j denotes I_j, $(-1)^j K_j$ or any linear combination of the two. By choosing $c=1$ and $z=1/\Delta^2$, (16) and (17) are identical; hence

$$u_j = AI_j + B(-1)^j K_j, \qquad (j=0, \pm1, \pm2\ldots), \quad (18)$$

where A and B are arbitrary constants. Note that z is real in this case. Figure 7 shows at $\Delta=1$, the behavior of AI_j in relation to the continuum solution (6) with both solutions normalized to having the same meridionally integrated zonal transport. While AI_j resembles the continuum solution, $(-1)^j K_j$ displays wildly growing grid-scale oscillations away from the equator. Whether this extra oscillatory mode is a problem in numerical models is investigated in section 7. To obtain a bounded solution, the K_j term is dropped in (18); hence

$$u_j = AI_j, \qquad (j=0, \pm1, \pm2\ldots). \quad (19)$$

The symmetry of the continuum solution (6) about the equator is also observed here as $u_j = AI_j = AI_{-j} = u_{-j}$. The percentage error of AI_j with respect to the continuum solution is also shown in Figure 4a, which shows that it is generally poorer than the C grid results, except when far away from the equator. Similarly, Figure 5 shows the E_1 (and A_1) grids to have larger zonally averaged rms errors in u and h than the other grids. To be fair to the E grid, we need to point out that the E grid (with spacing Δ in both dimensions) can be regarded as a B grid (with spacing $\sqrt{2}\Delta$) rotated by 45° (Figure 1). Hence in Figures 4 and 5, it may be more appropriate to compare the E grid of resolution D with the B and C grids with resolution $\sqrt{2}\Delta$. Such a comparison in Figure 5 would show the E_1 grid to be competitive with the C grids, but still not with the B grids.

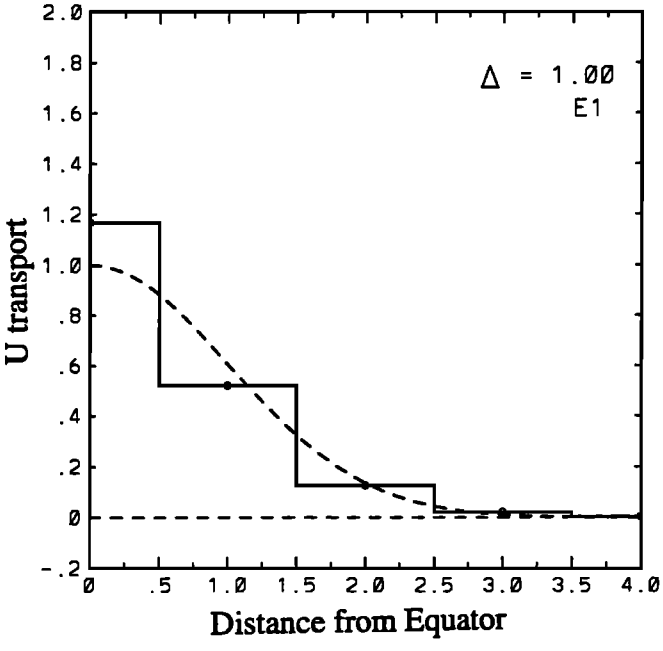

Figure 7. The zonal transport u as a function of the distance from the equator in the E_1 grid (solid curve) with the continnum solution shown as the dashed curve. The grid spacing $\Delta = 1$.

With the E_2 (and A_2) grids, where the u point no longer lies on the equator (Figure 6b), Equation (15) is replaced by

$$(j+\tfrac{1}{2})\Delta u_j = -\frac{(\eta_{j+1}-\eta_{j-1})}{2\Delta}, \quad (20)$$

leading to

$$u_{j+1} + \frac{2}{c}(j+\tfrac{1}{2})\Delta^2 u_j - u_{j-1} = 0, \qquad (j=0, \pm1, \pm2\ldots). \quad (21)$$

The recurrence relation of the modified Bessel functions again provides a hint. Consider

$$f_{j+1}(z) + \frac{2(j+\frac{1}{2})}{z} f_j(z) - f_{j-1}(z) = 0, \quad (j=0, \pm1, \pm2\ldots), \quad (22)$$

where the argument z may be complex. The two linearly independent solutions of (22) again involve the modified Bessel functions, though of fractional order, where $I_{j+\frac{1}{2}}$ and $I_{-j-\frac{1}{2}}$ are linearly independent. The general solution of (21) is

$$f_j = \sqrt{\pi/(2z)}\,(AI_{j+\frac{1}{2}} + BI_{-j-\frac{1}{2}}), \quad (23)$$

where A and B are arbitrary constants. The functions $\sqrt{\pi/(2z)}\,I_{j+\frac{1}{2}}$, $\sqrt{\pi/(2z)}\,I_{-j-\frac{1}{2}}$ are known as the modified spherical Bessel functions of the first and second kinds, respectively. For a solution of (21) symmetric about the equator, we choose $c=1$, $z=1/\Delta^2$ and $A=B$; hence

$$u_j = C(I_{j+\frac{1}{2}} + I_{-j-\frac{1}{2}}), \quad (24)$$

where the symmetry about the equator is easily seen from $u_0 = u_{-1} = C(I_{\frac{1}{2}} + I_{-\frac{1}{2}})$, $u_1 = u_{-2} = C(I_{\frac{3}{2}} + I_{-\frac{3}{2}})$, etc. Figure 8 plots the behavior of u_j on the E_2 grid at $\Delta = 0.3$, where the finite difference solution closely resembles the continuum solution near the equator, but develops large unbounded oscillations away from the equator. Reducing Δ does not eliminate the unbounded oscillations, but pushes their appearance further away from the equator. Increasing Δ leads to these unbounded oscillations moving closer to the equator, such that at, for instance, $\Delta=1$, the solution is unreasonable with oscillations right near the equator. Even though the C grid also has grid-scale oscillations (which do not grow spatially) for large enough Δ and far enough away from the equator, the situation for the E_2 case is much worse, as the oscillations grow rapidly spatially and are much closer to the equator for the same Δ. Thus an equatorially trapped Kelvin wave mode is not properly supported in the E_2 grid. For small Δ, the theoretically predicted spatially growing oscillations probably occur too far away from the equator to be a real problem. Of all the grids, only the E_2 and A_2 have no grid points on the equator at all, so for large enough Δ, the absence of grids at the equator is likely to cause serious problems for modeling the equatorial Kelvin wave. This strange phenomenon is investigated further in section 7.

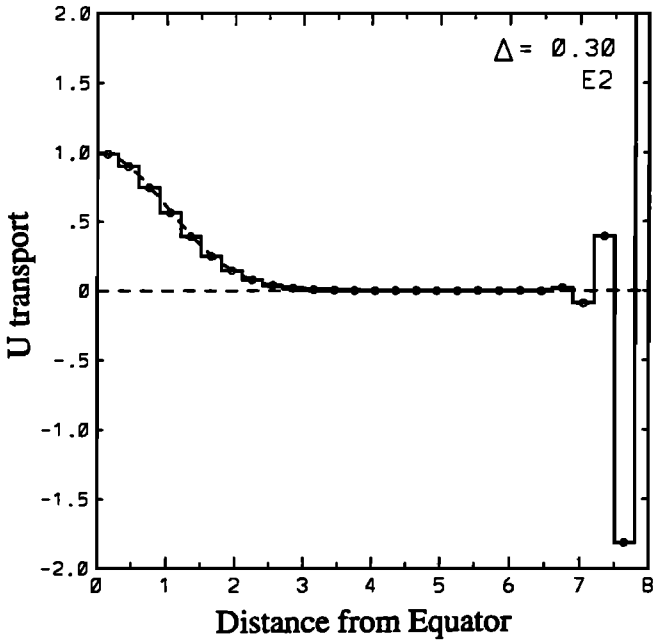

Figure 8. The zonal transport u as a function of the distance from the equator in the E_2 grid (solid curve) with the continuum solution shown as the dashed curve. The grid spacing $\Delta = 0.3$ (which is much smaller than the $\Delta = 1$ value used in Figures 3 and 7). Due to the divergence of the meridionally integrated zonal transport, the normalization used here is as follows: the E_2 solution is chosen to have the same u value as the continuum at the first point from the equator.

5. Equatorial Kelvin Waves on the B Grid

In contrast to the A, C, and E grids, the one-dimensional B grid (Figure 9) has the variables u and η at different latitudes. The finite difference equations are again formulated in two grid orientations, B_1 and B_2, where a u point lies on the equator in B_1, but an η point lies on the equator in B_2. The major difference from the previous cases of the A, C, and E grids is the breakdown of the $v = 0$ assumption here. Nonzero v terms need to be retained in both the mass and momentum equations, since the simple balances of (7) and (14) are no longer possible with u and η located at different latitudes. After considerable algebra, u and v can be eliminated, resulting in a recurrence relation for η on the B_1 grid:

$$\eta_{j+1} + F\eta_j + G\eta_{j-1} = 0, \tag{25a}$$

where
$$\begin{aligned} F = \{&2\omega^2(\omega k^2\Delta^2 + 4\omega - 2k\Delta^2 - 2\omega^3\Delta^2) \\ &+ \omega\Delta^2[j^2 + (j-1)^2](4\omega^2\Delta^2 - k^2\Delta^2 - 4) \\ &- 4\Delta^4 j(j-1)[k + \omega\Delta^2 j(j-1)]\} \\ &/[\omega(k^2\Delta^2 - 4)[\omega^2 - (j-1)^2\Delta^2]] \end{aligned}$$

$$G = (\omega^2 - j^2\Delta^2)/[\omega^2 - (j-1)^2\Delta^2]. \tag{25b}$$

The recurrence relation for η is of second order as in the E grid case, but the additional v terms render (25) a much more complicated problem. As we could not find an analytic solution for (25), we used a numerical approach based on the "shooting" method.

Given ω and Δ, we integrate (25a) northward starting from a point η_{-N} several Rossby radii south of the equator. Since the solution can be linearly scaled, η_{-N} can be arbitrarily fixed. To integrate (25a) northward, we need to make an initial guess of two parameters, the wavenumber k and η_{-N+1}, i.e., the η immediately north of η_{-N}. Both parameters could be complex. Equation (25a) is integrated to the northernmost point η_N, and a cost function is defined as the sum of η^2 over the few northernmost points. Since we are seeking an equatorially trapped solution, we minimize the cost function by adjusting k and η_{-N+1}. Since v was not eliminated, the recurrence relation (25) holds over the entire equatorial wave spectrum, which includes Rossby waves and gravity waves. Hence, the frequency ω is deliberately set low to avoid convergence to the gravity waves. A wave period of 130 days is chosen.

For the B_1 case, we found it necessary to allow the wavenumber to be complex. As Δ becomes small, the ratio of

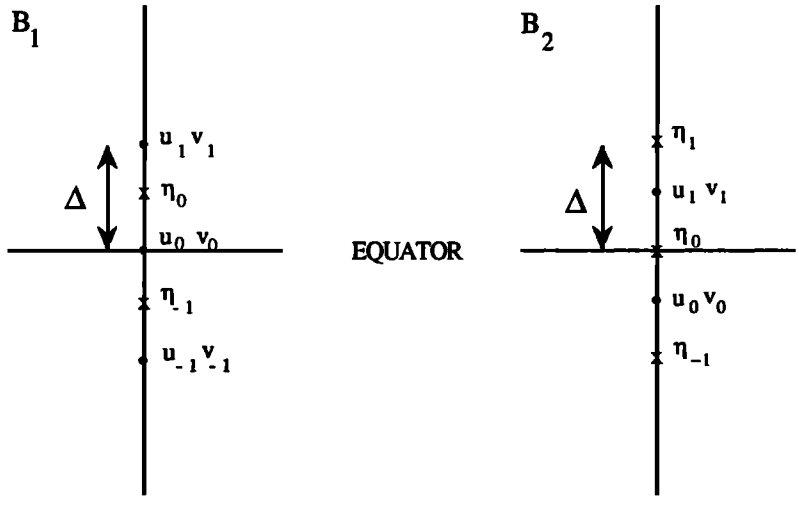

Figure 9. Two possible configurations of the B grid about the equator, henceforth referred to as the B_1 and B_2 grids, respectively.

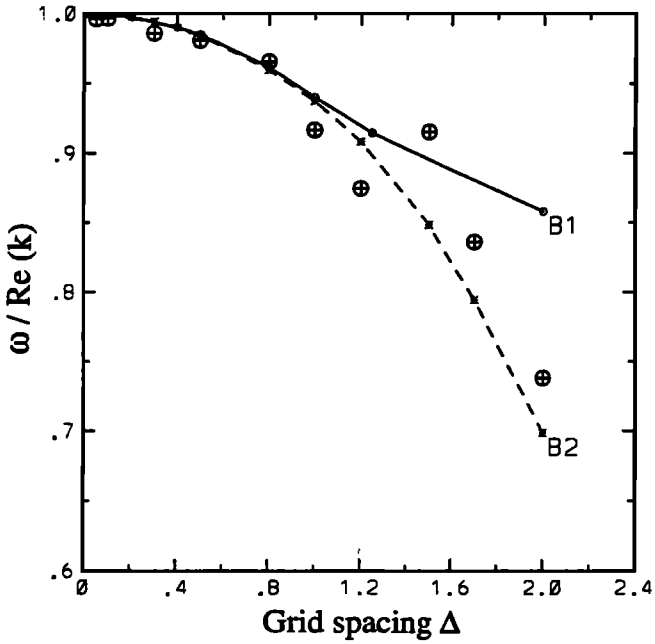

Figure 10. The phase speed c as a function of the grid resolution Δ for the B_1 grid (solid curve) and for the B_2 grid (dashed curve). Observed phase speed in shallow water equation models with the B_2 grid (see section 7) are also plotted as the circled crosses for comparison with the dashed curve.

the imaginary part to the real part of k converges to zero, while the real part of k converges to the wavenumber in the continuum solution, as expected. The imaginary part of k means that the Kelvin wave is zonally damped on the B_1 grid. At Δ=1, the 130-day period Kelvin wave has a zonal e-folding damping scale of 4.05×10^3 (Rossby radii), equivalent to about 29 times the Earth's circumference; hence the zonal damping is negligibly small. The phase speed c decreases as Δ increases (Figure 10), analogous to the behavior for coastal Kelvin waves on the B grid [*Hsieh et al.*, 1983]. Although the phase speed is dependent on Δ, the wave remains nondispersive (i.e., $\omega \propto k$). For the wave structure, the latitudinal variation of u transports is compared to that of the continuum counterpart (Figure 11a). Even though the "shooting" method did not guarantee a zonally symmetric solution, the numerical solution did turn out to be symmetric. In contrast to the C_{1a} and E_1 grid cases, the wave in B_1 is seen to be underestimated near the equator (Figure 4a). At regions away from the equator, the wave is widened, similar to the B grid coastal Kelvin wave [*Hsieh et al.*, 1983]. For the v transport, the ratio of v/u approaches zero as Δ tends to zero, as expected from the continuum theory. In general, v/u is too small to be noticeably different from zero.

For the B_2 case, eliminating u and v leads to

$$\eta_{j+1} + F\eta_j + G\eta_{j-1} = 0 \tag{26a}$$

where

$$\begin{aligned} F = \{&2\omega^2(\omega k^2\Delta^2 + 4\omega - 2k\Delta^2 - 2\omega^3\Delta^2) \\ &+ \omega\Delta^2[(j-\tfrac{1}{2})^2 + (j+\tfrac{1}{2})^2](4\omega^2\Delta^2 - k^2\Delta^2 - 4) \\ &- 4\Delta^4(j-\tfrac{1}{2})(j+\tfrac{1}{2})[k + \omega\Delta^2(j-\tfrac{1}{2})(j+\tfrac{1}{2})]\} \\ &/\{\omega(k^2\Delta^2 - 4)[\omega^2 - (j-\tfrac{1}{2})^2\Delta^2]\} \end{aligned}$$

$$G = [\omega^2 - (j+\tfrac{1}{2})^2\Delta^2]/[\omega^2 - (j-\tfrac{1}{2})^2\Delta^2]. \tag{26b}$$

The properties of the solution of (26) (Figures 9, 10b, 4b, and 5) are similar to those for the B_1 case, except that the wavenumber k now turns out to be real, meaning that the small zonal damping found in the B_1 grid is not present in the B_2 grid. The decline in the phase speed with worsening resolution is more severe in the B_2 grid than in B_1 (Figure 10). From Figure 5, the B_2 grid outperforms B_1, with the B grids generally superior to the A, C, and E grids in modeling u and η of the equatorial Kelvin wave.

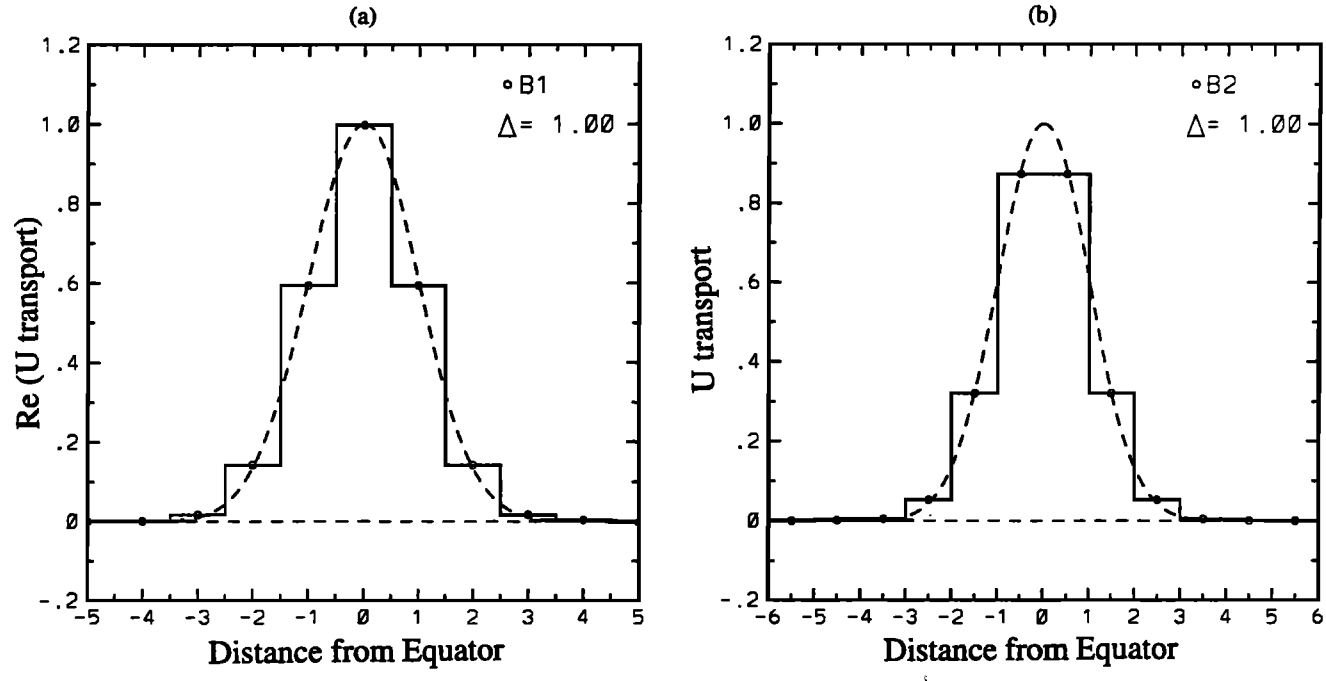

Figure 11. The zonal transport u as a function of the distance from the equator in the (a) B_1 grid and (b) B_2 grid, with the continnum solution shown as the dashed curve. The grid spacing $\Delta = 1$.

Since (25a) and (26a) are second order difference equations like (16), the B grid could also contain an extra spatially growing oscillatory mode like that in the E_1 grid. Unfortunately the cost function in our shooting method would only capture the bounded solutions for the B grid.

6. Zonal Heat Transport

The thermocline in the equatorial Pacific is normally tilted in the zonal direction, from about 200 m on the western Pacific to about 50 m in the eastern Pacific [*Philander*, 1990]. During an El Niño, an equatorial Kelvin wave traverses eastward across the Pacific, transmitting a large heat flux, while causing a deepening of the thermocline and an anomalous warming of the sea surface temperature in the eastern Pacific. An immediate application of the present theory is to calculate the zonal heat flux transmitted by the equatorial Kelvin wave in the various grids and to compare with the corresponding value in the continuum.

The meridionally and vertically integrated zonal heat transport (ZHT, measured in J/s) is defined (in dimensional variables) as

$$\text{ZHT} = \rho C_p \int_{y_1}^{y_2} [\int_D^0 uT dz] dy \tag{27}$$

where T is the temperature, ρ and C_p are the density and specific heat of water, respectively, y_1 and y_2 are latitudinal limits of integration, and D is the ocean depth. For simplicity, consider a two-layer model, with subscripts 1 and 2 denoting the first and second layers. The vertical integral term in (27) becomes

$$\int_D^0 uT dz = u_1 T_1 (H_1 - h) + u_2 T_2 (H_2 + h), \tag{28}$$

where both temperature and velocity are constant throughout each layer, H_i is the equilibrium water depth in layer i, and h is the interface elevation. Substituting (28) into (27),

$$\begin{aligned}\text{ZHT} = \rho C_p [&T_1 H_1 \int_{y_1}^{y_2} u_1 \, dy - T_1 \int_{y_1}^{y_2} u_1 h \, dy \\ &+ T_2 H_2 \int_{y_1}^{y_2} u_2 \, dy + T_2 \int_{y_1}^{y_2} u_2 h \, dy].\end{aligned} \tag{29}$$

These dimensional variables are related to the nondimensional variables u and η by

$$u_1 = -\frac{H_2}{H_1 + H_2} c' u, \quad u_2 = \frac{H_1}{H_1 + H_2} c' u, \quad h = H\eta, \tag{30}$$

with H the equivalent depth and c' the wave speed defined as

$$H = \frac{H_1 H_2}{H_1 + H_2}, \quad c' = \sqrt{g' H}. \tag{31}$$

With $\eta = u$ in the continuum as well as the A, C, and E grids, (29) can be expressed as

$$\text{ZHT} = \rho C_p L c' \{-T_1 H \mathbf{I}_1 + T_1 \frac{H^2}{H_1} \mathbf{I}_2 + T_2 H \mathbf{I}_1 + T_2 \frac{H^2}{H_2} \mathbf{I}_2\}, \tag{32}$$

where L, the length scale, is the equatorial Rossby radius, and the nondimensional integrals are

$$\mathbf{I}_1 = \int_{y_1}^{y_2} u \, dy, \quad \mathbf{I}_2 = \int_{y_1}^{y_2} u^2 dy. \tag{33}$$

Taking $u = u(y)\cos(kx - \omega t)$ and averaging over one wave period and one wavelength, we obtain

$$\langle \mathbf{I}_1 \rangle = 0, \quad \langle \mathbf{I}_2 \rangle = \tfrac{1}{2} \int_{y_1}^{y_2} u^2(y) dy. \tag{34}$$

Mean ZHT is obtained from (32) and (34) where $u(y)$ is computed from the continuum solution (6) or from one of the C or E grid solutions. The integration in (34) is computed to ±8 Rossby radii away from the equator.

For the B grid, since $\eta \neq u$, the integrals $\mathbf{I}_2$ in (32) are replaced by $\mathbf{I}_3$, where

$$\mathbf{I}_3 = \int_{y_1}^{y_2} u\eta \, dy, \quad \langle \mathbf{I}_3 \rangle = \tfrac{1}{2} \int_{y_1}^{y_2} u(y)\eta(y) \, dy \tag{35}$$

The model parameters used to evaluate the ZHT in (32) are $g' = 0.02$ m s^{-2}, $H_1 = 200$ m, $H_2 = 4000$ m, $T_1 = 303^o$K, and $T_2 = 290^o$K. The pre-El Niño situation in the equatorial Pacific has the interface on the western boundary lowered (i.e., a trough) and that at the eastern boundary raised (a "crest"). During an El Niño, the "trough" propagates from the western boundary to the eastern boundary in about 2 months. This suggests that the El Niño scenario can be represented in our simple two-layer model by an equatorial Kelvin wave with a wavelength double that of the zonal basin width and a period of about 4 months (we chose 130 days). Figure 12 shows the percentage error in the ZHT on the four C grids, the E_1, the B_1, and the B_2 grids with respect to the ZHT in the continuum. The ZHT on the E_2 grid is not considered here as this solution was found to be unbounded in the last section. Note that the ZHT values in Figure 12 were calculated based on the assumption that the meridionally integrated u transports in the finite difference models were the same as the transport in the continuum solution. Under this normalization assumption, C_{1b}, C_{2b}, B_1, and B_2 all underestimated the ZHT, while C_{1a}, C_{2a}, and E_1 overestimated the ZHT relative

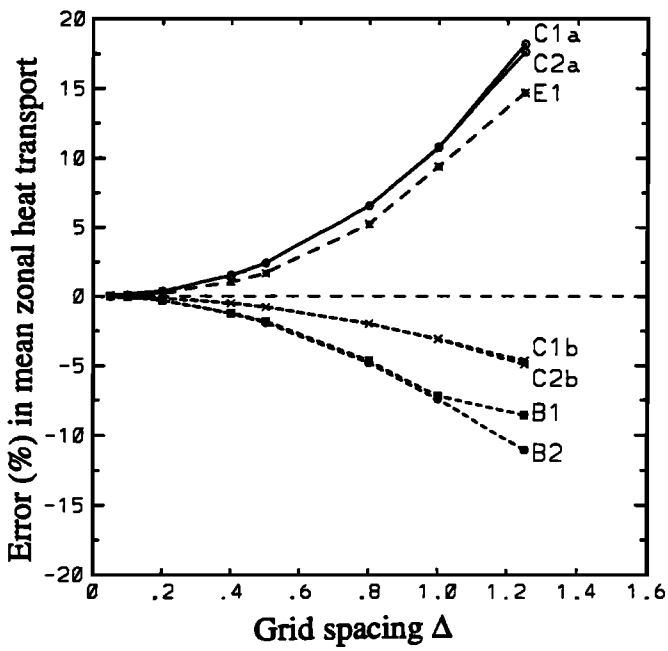

Figure 12. The percentage error in the mean zonal heat transport of the finite differenced equatorial Kelvin wave (with respect to that in the continuum) plotted as a function of the grid spacing Δ on the four C grids, the E_1, the B_1 and B_2 grids. The frequency and wavenumber of the Kelvin wave were chosen to be representative of the Kelvin wave during a typical El Niño.

to the continuum solution. In general, the best ZHTs were found in C_{1b}, C_{2b}, followed by B_1 and B_2, in decreasing order of accuracy. It may seem puzzling why the B grid, which models the currents and sea level displacements better than the C grid, turns out to be less accurate in the ZHT. This may be explained by the fact that for the C grid, u and η are located at the same latitude, while for the B grid, they are not. Since the product $u\eta$ is involved in calculating the ZHT, the B grid is at a disadvantage when its u and η points are at different latitudes. Again as in Figure 5, the result for E_1 at resolution Δ should probably be compared with the other grids at resolution $\sqrt{2}\Delta$, which gives E_1 a good accuracy for ZHT.

7. Numerical Experiments

To experimentally verify our theoretical predictions of finite difference effects, we ran shallow-water equation models [*Arakawa and Lamb*, 1977] on the various grids, with absolutely no damping. Centered on the equator, the numerical models were 12 Rossby radii wide meridionally, and 38 Rossby radii wide zonally (corresponding to about 11,000 km), with solid boundaries all around. The initial condition corresponded to having an equatorial Kelvin wave (with half wavelength equal to the model zonal width). Zonally, the wave had a sinusoial shape with a crest centered in the middle of the ocean. Our finite difference theory provided the initial sea level displacement and currents for this wave. The wave was allowed to evolve without external forcing. As the wave propogated eastward, we observed the shape and measured the propagation speed.

Our theoretical prediction of decreasing phase speed in the B grid with worsening resolution was indeed observed. Figure 10 shows some experimentally measured phase speeds plotted against the theoretical phase speed on the B_2 grid. Similarly, our predictions that the phase speed should remain unchanged in the C grid with worsening resolution was also confirmed, with Figure 13 showing some measured phase speeds on the C_{2b} grid.

We also used the continuum solution (Section 2) as the initial condition on these grids. However, as the continuum solution is not the correct Kelvin wave mode on these grids, the initial wave soon began to disperse at a significantly faster rate than in the corresponding run which used our theoretical finite difference wave solution as the initial condition.

Our predictions for the A or E grids were also tested on shallow-water A grid models. As the resolution worsens, the observed phase speed on the A_1 grid became greater than our predictions (which was a constant independent of the grid spacing) (Figure 13). The spatially growing grid-scale oscillatory mode permitted under (18) was not observed, indicating that the mode was not readily excited. However, our runs were only of 1-month duration, which could be too short a time to excite such a mode. In practice, numerical models would have damping terms which would also control this oscillatory mode. For the A_2 case, where there is no true equatorially trapped Kelvin mode, we could only run with the continuum solution as the initial condition. At coarse resolution, the results were a significantly stronger dispersion of the original wave and a drastic decline in the phase speed (shown as the circled crosses in Figure 13). The sharp decline in the phase speed was likely caused by the scattering of the initial wave form into the other equatorial

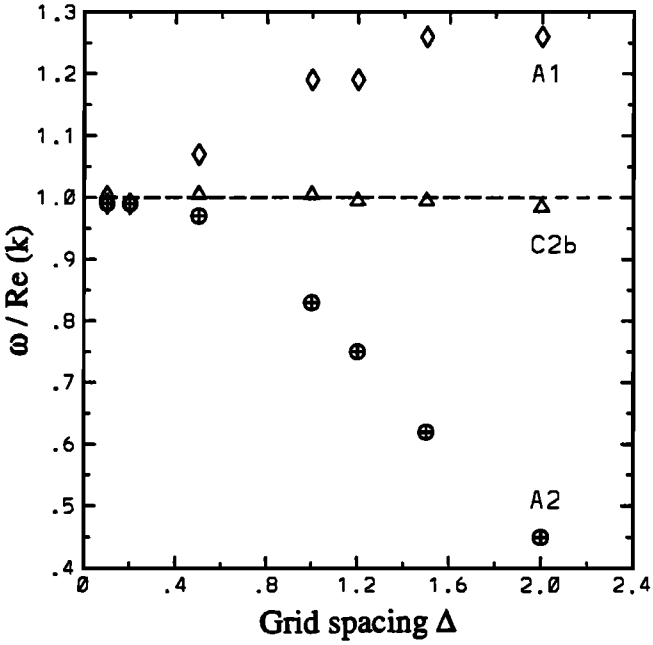

Figure 13. Observed phase speeds in shallow water equation models as a function of the grid spacing Δ for the A_1 grid (diamond symbols), the A_2 grid (circled crosses), and the C_{2b} grid (triangles). The theoretical phase speed is plotted as the dashed horizontal line.

modes, such as the westward propagating Rossby modes, which would produce the low observed phase speed. For finer resolution, the growing oscillations in our theory (Figure 8) occur too far off the equator to be of real consequence in our numerical model, and the initial Kelvin wave propagated without much deviation from the continuum solution.

8. Summary and Conclusion

We have derived exact analytic solutions for the free equatorial Kelvin wave on the Arakawa A, C, and E grids. By ignoring the finite difference effects in the zonal direction, the A grid solutions are identical to the E grid solutions. The $v = 0$ assumption for the Kelvin wave in the continuum also holds on the A, C, and E grids. The B grid is very different from the A, C, and E grids in that the u and η points do not lie on the same latitude in the B grid, so that a direct relation between u and η, such as (7), is not possible in the B grid, rendering a need for a nonzero v to balance the momentum and mass equations. Our main findings for the equatorial Kelvin wave on the A, C, and E grids are as follows.

1. The dispersion relations for the finite difference Kelvin wave are identical to the dispersion relation in the continuum, for both undamped and damped waves (see appendix).

2. For the C grid, a better solution is obtained by calculating the Coriolis term in the v-transport equation by latitudinally averaging the yu term (method b) than by multiplying y at the v latitude to the latitudinal average of two u points (method a), though method a probably has superior stability [*Sadourny*, 1975a,b].

3. The E grid with a u point on the equator (i.e., E_1), allows an extra grid-scale oscillatory mode besides the Kelvin mode. However, the grid-scale mode does not appear readily excited. The E grid without a grid point on the equator (i.e., E_2) does

not properly support an equatorially trapped Kelvin mode, thus energy would leak to other equatorial modes.

The main results for the B grid are as follows.

1. Phase speed for the Kelvin wave decreases with worsening resolution (i.e., increasing Δ). However, the dispersion relation remains nondispersive (i.e., $\omega \propto k$).

2. On B_1 (with u point on the equator), there is a small zonal damping arising from the finite difference effect, which is absent in the B_2 configuration.

3. Parameter ν is generally nonzero, and only satisfies $\nu \to 0$ as $\Delta \to 0$. In general, ν/u is negligibly small.

4. Among the A, B, C, and E grids, the B grid appears to model the currents and sea level displacements of the equatorial Kelvin wave best under coarse resolution, with the B_2 configuration slightly better than B_1. However, in terms of zonal heat transport and phase speed, the C_{2b} and C_{1b} grids are better.

Appendix: Damped Equatorial Kelvin Waves

We now succinctly examine the equatorial Kelvin wave with damping terms in the governing equations. The zonal flow equations with damping are given by (2). Again assuming a plane wave form (4), it follows that

$$u(y) = u_0 \exp[-\sqrt{(\omega+i\gamma)/(\omega+i\varepsilon)}\, y^2/2] \qquad \text{(A1)}$$

and

$$\eta(y) = u_0\sqrt{(\omega+i\varepsilon)/(\omega+i\gamma)}\exp[-\sqrt{(\omega+i\gamma)/(\omega+i\varepsilon)}\, y^2/2] \qquad \text{(A2)}$$

with u_0 and $u_0\sqrt{(\omega+i\varepsilon)/(\omega+i\gamma)}$ the wave amplitudes for u and η, respectively, at the equator [see *Yamagata and Philander*, 1985]. They found that increasing ε widens the Kelvin wave in the meridional direction, while in contrast, increasing γ concentrates the wave around the equator. The dispersion relation is

$$k^2 = \omega^2 + i(\gamma+\varepsilon)\omega - \varepsilon\gamma \qquad \text{(A3)}$$

Thus Rayleigh friction and Newtonian cooling disperse the wave. By assuming free wave (i.e., ω real), (A3) implies wave damping in the zonal direction. With ω set at a wave period of 130 days, the zonal phase speed, $\omega/\mathrm{Re}(k)$, is shown in Figure A1, where an interesting cancellation effect between γ and ε is observed. For instance, with $\varepsilon = 0$, increasing γ leads to a drop in the zonal phase speed, as expected. However, if ε is raised, it begins to cancel the slow-down effect due to γ, such that when $\varepsilon = \gamma$, the phase speed has returned to 1, as if both γ and ε were zero. Further increasing ε again leads to a drop in the phase speed, as illustrated by the curve labelled $\varepsilon = 5\gamma$. The damping parameters ε and γ also produce phase shifts in the meridional direction, as seen from (A1) and (A2). The constant phase lines in the x-y plane are described by

$$-Im\left[\sqrt{(\omega+i\gamma)/(\omega+i\varepsilon)}\right]y^2/2 + Re(k)x = \text{const.} \qquad \text{(A4)}$$

To the order of $O(\varepsilon/\omega, \gamma/\omega)$, the imaginary part of the term in brackets in (A4) is directly proportional to $(\gamma-\varepsilon)$, thereby revealing the cancellation effect between γ and ε. The phase lines (which were aligned in the meridional direction in the undamped case) may now slant backwards or forwards from the equator, depending on the relative size of ε and γ, as discussed by *Yamagata and Philander* [1985]. For $\varepsilon = \gamma$ or $\omega = 0$, (A4) implies that the phase lines are aligned in the meridional direction, as in the undamped case. Also from (A1) and (A2), it is clear that for the particular case of $\varepsilon = \gamma$, the meridional structures of u and η are reduced to the undamped solution.

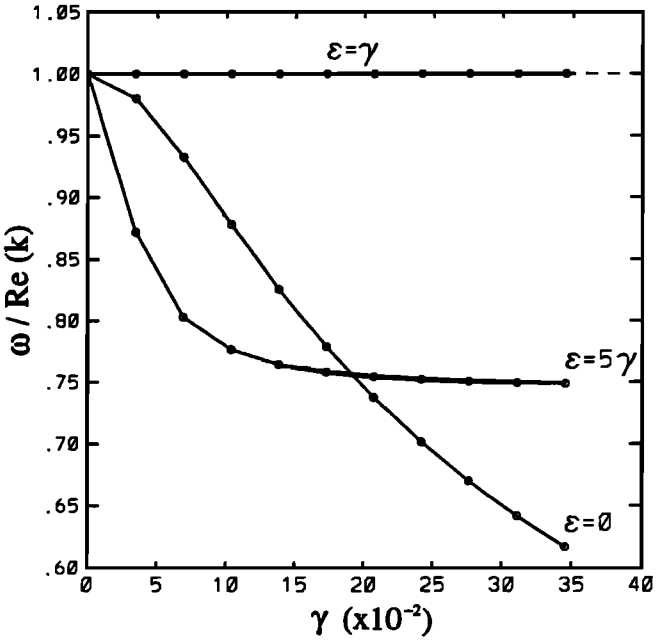

Figure A1. The zonal phase speed $\omega/Re(k)$ plotted as a function of γ for various values of ε.

For the C grid, we limit ourselves to the C_{2b} case, with the finite difference form of (2) yielding

$$(\omega+i\varepsilon)u_j = k\eta_j, \quad \tfrac{1}{2}\Delta^2[(j+\tfrac{1}{2})u_j + (j-\tfrac{1}{2})u_{j-1}] = \eta_{j-1} - \eta_j,$$
$$(\omega+i\gamma)\eta_j = ku_j. \qquad \text{(A5)}$$

The first and third equations in (A5) combine to give the dispersion relation, which is easily shown to be identical to the continuum dispersion relation (A3) and is therefore independent of Δ. The meridional structure is obtained by combining the first two equations in (A5):

$$u_j = \left[\frac{1-(j-\tfrac{1}{2})k\Delta^2/2(\omega+i\varepsilon)}{1+(j+\tfrac{1}{2})k\Delta^2/2(\omega+i\varepsilon)}\right]u_{j-1}, \qquad \text{(A6)}$$

case C_{2b}. As u is now complex, there is an additional phase shift in the meridional direction. We choose to plot the meridional profile of $Re(u)$ in Figure A2 at resolution Δ=1, with the curve again normalized to have the same meridionally integrated zonal transport as in the continuum case. The plot is generated for a wave period of 130 days with (dimensionalized) $\varepsilon = 1/50$ day^{-1} and $\gamma = 1/10$ day^{-1}, typical values used by *Yamagata and Philander* [1985]. A weak reverse flow is found at 2.5 Rossby radius from the equator. The corresponding undamped solution (from Figure 3b) is superimposed as the short-dashed curves for comparison.

The finite differenced equations with respect to the E_1 grid are

$$(\omega+i\varepsilon)u_j = k\eta_j, \quad j\Delta u_j = -\left(\frac{\eta_{j+1}-\eta_{j-1}}{2\Delta}\right), \qquad \text{(A7)}$$
$$(\omega+i\gamma)\eta_j = ku_j.$$

The dispersion relation is again found to be identical to (A3), while the meridional structure is described by

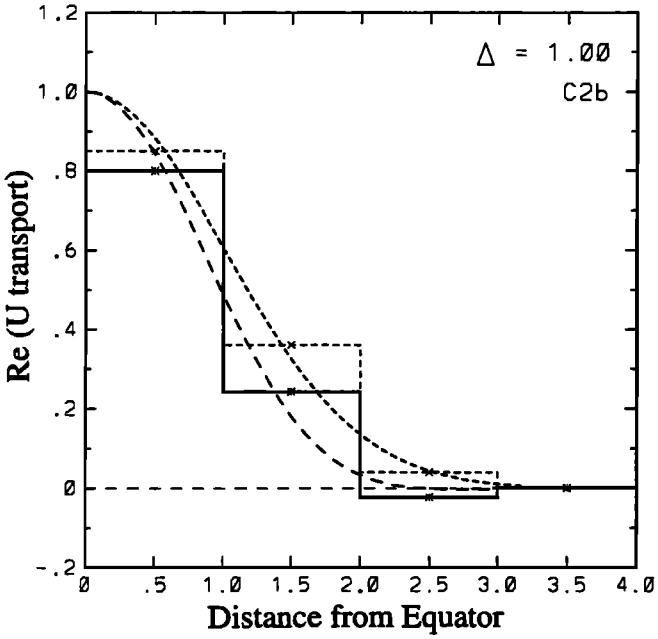

Figure A2. $Re(u)$ for the C_{2b} grid plotted as a function of the distance from the equator. The solid curve shows the C_{2b} solution for nonzero γ and ε (as given in the text), with the corresponding continuum solution as the long-dashed curve. The corresponding undamped ($\gamma = \varepsilon = 0$) finite difference and continuum solutions are also shown by the short-dashed curves. In the damped case, we have chosen $\gamma > \varepsilon$; hence the damped continuum solution (long-dashed curve) is more concentrated around the equator than the invisicid continuum solution (short-dashed curve). (If $\gamma < \varepsilon$ were chosen, the damped continuum solution would be wider than the undamped continuum solution.)

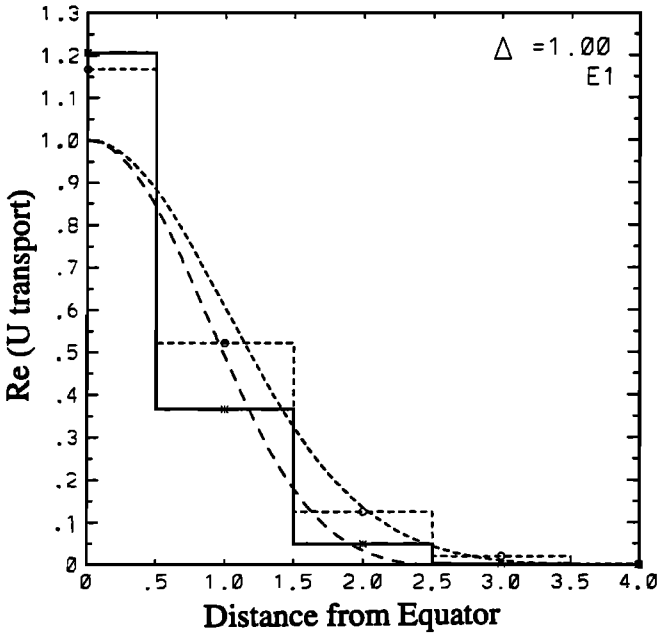

Figure A3. $Re(u)$ for the E_1 grid plotted as a function of the distance from the equator. The solid curve shows the E_1 solution for nonzero γ and ε (as given in the text), with the corresponding continuum solution as the long-dashed curve. The corresponding undamped ($\gamma = \varepsilon = 0$) finite difference and continuum solutions are also shown by the short-dashed curves.

$$u_{j+1} + 2j\Delta^2\left(\frac{\omega+i\gamma}{k}\right)u_j - u_{j-1} = 0, \quad (j = 0,\pm1,\pm2,\ldots). \tag{A8}$$

Equation (A8) resembles (16) in the undamped case except for the damping effect $i\gamma$ appearing now in the second term. The effect from ε is exerted implicitly in (A8) via ω and k through the dispersion relation (A3).

Following the same line of argument as in the undamped case, solutions of (A8) can be written in terms of the modified Bessel functions except that the function' s argument is now complex. Hence,

$$u_j(z) = A I_j(z), \quad , \quad z = \frac{k}{\omega+i\gamma}\,\frac{1}{\Delta^2} \tag{A9}$$

and from (A7),

$$\eta_j(z) = A\frac{\omega+i\varepsilon}{k} I_j(z) = A\sqrt{\frac{\omega+i\varepsilon}{\omega+i\gamma}}\, I_j(z). \tag{A10}$$

The meridional structure of $Re(u)$ in (A9) is shown in Figure A3 for Δ=1.

In summary, as η and v lie on the same latitude in all the C and E grid configurations, their dispersion relations are identical to that for the continuum, i.e. (A3). For the B grids, one can derive analogous equations to (25) and (26), though the functions F and G will be complex, and a numerical approach will again be needed.

Acknowledgments. This research was supported by the Canadian Natural Sciences and Engineering Research Council through the Canadian WOCE project and the research grant to W. Hsieh.

References

Abramowitz, M., and I. A. Stegun, *Handbook of Mathematical Functions.*, 1046 pp., Dover, New York, 1972.

Arakawa, A., and V. R. Lamb, *Computational Design of the Basic Dynamical Processes of the UCLA General Circulation Model.*, pp. 173-265, Academic, San Diego, Calif., 1977.

Batteen, M. L., and Y. J. Han, On the computational noise of finite difference schemes used in ocean models, *Tellus, 33,* 387-396, 1981.

Bleck, R., and D. B. Boudra, Initial testing of a numerical ocean circulation model using a hybrid (quasi-isopycnic) vertical coordinate, *J. Phys. Oceanogr., 11*(6), 755-770, 1981.

Blumberg, A. F., and G. L. Mellor, Diagnostic and prognostic numerical circulation studies of the South Atlantic Bight, *J. Geophys. Res.*, 88(C8), 4579-4592, 1983.

Bryan, K., and M. D. Cox, A numerical investigation of the oceanic general circulation, *Tellus , 19,* 54-80, 1967.

Dietrich, D. E., M. G. Marietta, and P. J. Roache, An ocean modelling system with turbulent boundary layers and topography, Numerical description, *Int. J. Numer. Methods Fluids , 7,* 833-855, 1987.

Foreman, M. G. G., An accuracy analysis of selected finite difference methods for shelf waves, *Continental Shelf Res., 7*(7), 773-803, 1987.

Gill, A. E., *Atmosphere-Ocean Dynamics*, 662 pp., Academic, San Diego, Calif., 1982.

Haidvogel, D. B., J. L. Wilkin, and R. Young, A semi-spectral primitive equation ocean circulation model using vertical sigma and orthogonal curvilinear horizontal coordinates, *J. Comput. Phys., 94*(1), 151-185, 1991.

Henry, R. F., Richardson-Sielecki schemes for the shallow-water equations, with applications to Kelvin waves, *J. Comput. Phys., 41*(2), 389-406, 1981.

Hsieh, W. W., M. K. Davey, and R. C. Wajsowicz, The free Kelvin wave in finite difference numerical models, *J. Phys. Oceanogr.*, *13*(8), 1383-1397, 1983.

Maier-Reimer, E., and K. Hasselmann, Transport and storage of CO_2 in the ocean-- An inorganic ocean-circulation carbon cycle model, *Clim. Dyn.*, *2*, 63-90, 1987.

McCreary, J., A linear stratified ocean model of the equatorial undercurrent, *Philos. Trans. R. Soc. London A*, *298*, 603-635, 1981.

Oberhuber, J. M., Simulation of the Atlantic circulation with a coupled sea ice-mixed layer-isopycnal general circulation model, *Rep. 59*, Max-Planck-Inst. fur Meteorol., Hamburg, Germany, 1990.

O'Brien, J. J., and F. Parham, Equatorial Kelvin waves do not vanish, *Mon. Weather. Rev.*, *120*, 1764-1766, 1992.

Philander, S. G., *El Niño, La Niña, and the Southern Oscillation.*, 289 pp., Academic, San Diego, Calif., 289 pp., 1990.

Sadourny, R., The dynamics of finite difference models of the shallow-water equations, *J. Atmos. Sci.*, *32*, 680-689, 1975a.

Sadourny, R., Compressible model flows on the sphere, *J. Atmos. Sci.*, *32*, 2103-2110, 1975b.

Wajsowicz, R. C., Free planetary waves in finite difference numerical models, *J. Phys. Oceanogr.*, *16*(4), 773-789, 1986.

Yamagata, T., and S. G. H. Philander, The role of damped equatorial waves in the oceanic response to winds, *J. Oceanogr. Soc. Jpn.*, *41*(5), 345-357, 1985.

W. W. Hsieh and M. K. F. Ng, Department of Oceanography, University of British Columbia, Vancouver, B. C., Canada V6T 1Z4.

(Received September 3, 1992; revised August 19, 1993; accepted September 27, 1993.)